JOURNAL OF THERMOPHYSICS AND HEAT TRANSFER
Vol. 21, No. 3, July–September 2007

Heat Transfer in a Reciprocating Thermosyphon Fitted with Staggered Transverse Ribs

Shyy Woei Chang*
National Kaohsiung Marine University, Kaohsiung 811, Taiwan, Republic of China
W. David Morris†
University of Wales, Swansea, SA28PP Wales, United Kingdom
Tong-Minn Liou‡
National Tsing Hua University, Hsinchu 300, Taiwan, Republic of China
and
Shyr Fuu Chiou§
National Kaohsiung Marine University, Kaohsiung City 81143, Taiwan, Republic of China

DOI: 10.2514/1.28131

This paper describes an experimental investigation of heat transfer in a reciprocating antigravity open thermosyphon. The thermosyphon tube is square in cross section, and two opposite walls are roughened with staggered transverse ribs. This flow/heat-transfer system has relevance, as a fundamental study, to the *shaker*-cooling system for the pistons of reciprocating engines. A series of experiments are undertaken to demonstrate the complex interaction that exists between inertial, reciprocating, and buoyancy forces on the performance of this form of cooling system. It is shown that reciprocation of the system significantly improves heat transfer in comparison with the stationary antigravity thermosyphon performance. The buoyancy effects from gravity and reciprocation improve heat transfer. Reductions in the effectiveness of buoyancy forces are produced when the relative strengths of inertial or/and pulsating forces increase. In the extrapolated case of zero buoyancy, it was found that the local heat transfer along the thermosyphon tube was reduced in comparison to the static case at relatively low levels of reciprocation frequency. As the reciprocation frequency was increased, this effect was reversed and heat transfer improved in comparison with the stationary case.

Nomenclature

A	=	correlation coefficients
A_s	=	entire heated surface area of the thermosyphon tube, m^2
a	=	crank radius (reciprocating amplitude), m
C_p	=	specific heat of coolant, $J \cdot kg^{-1} \cdot K^{-1}$
d	=	hydraulic diameter of the test duct, m
e	=	rib height, m
F	=	reciprocating frequency, Hz
Gr_g	=	gravitational Grashof number, $g\beta_0 d^3 \Delta T_f / \nu_0^2$
Gr_p	=	reciprocating Grashof number, $a\omega^2 \beta_0 d^3 \Delta T_f / \nu_0^2$
g	=	gravitational acceleration, $m \cdot s^{-2}$
H	=	height of the thermosyphon, m
Hp	=	height of the plenum chamber, m
h	=	local convective heat-transfer coefficient, $W \cdot m^{-2} \cdot K^{-1}$
k	=	thermal conductivity of coolant, $W \cdot m^{-1} \cdot K^{-1}$
l	=	land of the rib, m
$\dot{m}$	=	total amount of mass flow rate fed into the reciprocating system, $kg \cdot s^{-1}$
Nu	=	reciprocating Nusselt number, $hd/k_{f,0}$
Nu_0	=	nonreciprocating Nusselt number
n	=	exponent of exponential function in Nu/Nu_0 correlation
P	=	dimensionless flow pressure, $p/\rho w_m^2$
Pi	=	pitch of the ribs, m
Pr	=	Prandtl number, $\mu C_{p,0}/k_{f,0}$
Pu	=	pulsating number, $\omega d/w_m$
p	=	flow pressure, $N \cdot m^{-2}$
p'	=	pressure perturbation from hydrostatic pressure of reciprocating flow, $N \cdot m^{-2}$
Q	=	heating power transferred into the thermosyphon, W
q	=	local convective heat flux, $W \cdot m^{-2}$
Re	=	$\rho_0 w_m d/\mu_0$
T	=	fluid temperature, °C
T_0	=	temperature at the entrance of the thermosyphon, °C
$\boldsymbol{U}, \boldsymbol{V}, \boldsymbol{W}$	=	dimensionless flow velocity vectors, $(u, v, w)/w_m$
u, v, w	=	flow velocities, $m \cdot s^{-1}$
Wd	=	width of the plenum chamber, m
w_m	=	reference flow velocity, $m \cdot s^{-1}$, $\dot{m}/(\rho_0 d^2)$
x, y, z	=	coordinates, m
X, Y, Z	=	dimensionless coordinates $(x, y, z/d)$
α, γ	=	functional coefficients of heat-transfer correlation for the static thermosyphon
β	=	thermal expansion coefficient of coolant, K^{-1}
η	=	nondimensional temperature
μ	=	dynamic viscosity of coolant, $kg \cdot s^{-1} \cdot m^{-1}$
ν	=	kinetic viscosity of coolant, μ/ρ
ρ	=	coolant density, $kg \cdot m^{-3}$
τ	=	dimensionless time, ωt
φ	=	unknown functions
χ	=	dimensionless flow pressure
ω	=	angular velocity of rotating disc creating reciprocating motion, rad^{-1}

Subscripts

f	=	fluid
w	=	wall condition

Received 1 October 2006; revision received 28 January 2007; accepted for publication 2 February 2007. Copyright © 2007 by the American Institute of Aeronautics and Astronautics, Inc. All rights reserved. Copies of this paper may be made for personal or internal use, on condition that the copier pay the $10.00 per-copy fee to the Copyright Clearance Center, Inc., 222 Rosewood Drive, Danvers, MA 01923; include the code 0887-8722/07 $10.00 in correspondence with the CCC.

*Professor, Thermal Fluids Laboratory; swchang@mail.nkmu.edu.tw.
†Research Professor, Department of Mechanical Engineering, Swansea Singleton Park; w.d.morris@swansea.ac.uk.
‡Professor, Department of Power Mechanical Engineering; tmliou@nthu.edu.tw.
§Lecturer, Department of Marine Engineering, No. 142, Haijhuan Road; sfchiou@mail.nkmu.edu.tw.

ZB = zero-buoyancy condition
0 = reference condition at temperature T_0

Introduction

THE thermodynamic advantages obtained by operating heavy-duty marine diesel engines with a high compression ratio and maximum combustion temperature stimulate an active quest for improving performance and economy. To obviate the need for heavy-duty reduction gearboxes with an attendant reduction in weight, the propeller is directly driven by the propulsion diesel engine. Therefore, a larger-than-normal stroke-to-bore ratio is required to achieve the low engine speed required to match the characteristics of the engine to the directly driven propeller. However, the use of a high stroke-to-bore ratio combined with a high compression ratio and high combustion temperature greatly increases the thermal and mechanic loads imposed on the piston. Therefore, intensive piston cooling is necessary if the mechanical integrity and life of the engines are to be maintained at a commercially realistic level.

A variety of piston-cooling schemes have used internal forced convection, impingement, and the so-called *shaker/bore*-cooling concepts. Figure 1 typifies the multibore shaker-cooling systems in the pistons of the Sulzer RTA diesel engine series. As shown, the coolant in each of these blind passages is convected from and to the plenum chamber in the tubewise direction when the piston reciprocates. Penetrations of coolant into the blind passages are facilitated by the vortical cells in the blind tube [1] and by the impinging jet for the convective and impinging shaker-bore systems, respectively. The plenum chamber acts as reservoir that provides a thermal sink for the coolant in the blind bores to exchange heat with the bulk flow in the plenum chamber. Because the tubewise directions of the inclined blind bores are no longer parallel to the reciprocating forces, temporally varying cross-plane secondary flows are also induced.

Studies of static open-cavity flows have demonstrated that the penetration of coolant in each blind passage is influenced by the flow pattern across its open surface and also by the geometrical features of

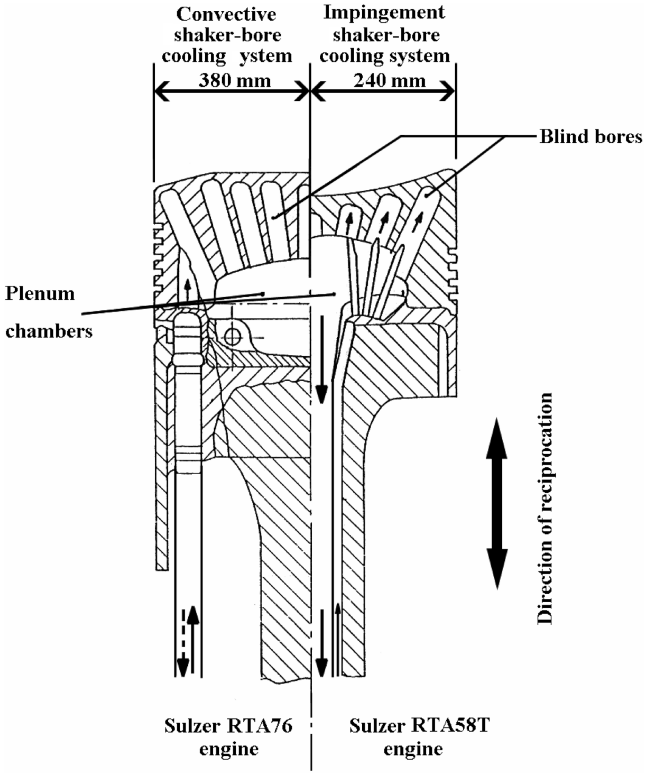

Fig. 1 Multibore shaker-cooling system in the pistons of the Sulzer RTA diesel engine series.

the passage and the plenum chamber [2,3]. Decreasing the aspect ratio of the cavity (i.e., a deeper cavity) generally increases the vortices formed in the passage and weakens the vortex in the vicinity of the sealed end [4]. During the transient development of the flow over the open cavity, the rate of mass exchange of the fluid inside the cavity is enhanced [4]. When the periodicity of the buoyancy forces in the closed cavity flow is introduced (either by the periodical heating condition [5,6] or by the vibration of solid boundary), rich vortical flow structures are established in these enclosures [7]. The processes of vortex generation, convection, and diffusion for these enclosed flows are dynamic and depend on the oscillating frequency and amplitude of the boundary conditions imposed [6–9]. In general, buoyancy effects induced by vibration improve heat transfer.

Studies of enclosed flows that involve vibrational buoyancy [5–12] share a degree of similarity with the cooling geometry depicted in Fig. 1. However, subtle differences exist between the reciprocating forces and the flow interactions initiated in the open-ended region of each blind bore of the piston shaker-cooling networks. Because the sealed end of the piston-cooling passage is vertically above the entrance to the coolant reservoir, there is a tendency for the coolant to stratify, with regions of hot coolant *trapped* in the vicinity of the sealed end due to gravitational free convection when the system is static. This class of flow system has been referred to as an *antigravity open free-convection thermosyphon* in the technical literature. The additional superimposed effect of reciprocation on the system has led to the piston shaker-cooling method being categorized as a *reciprocating antigravity open thermosyphon*.

It is well known that the performance of internal cooling passages for the more critical components of a power plant may be improved by the use of artificially roughened surfaces. In this respect, the use of ribs or fins is particularly attractive. Thus, the performance of the piston shaker-cooling method could be further enhanced if some form of ribbing was applied to the internal surfaces of the thermosyphon tubes. Although the use of surface ribs has been a subject of much fundamental research over the years ([13–15], for example), few research investigations of the flow and heat transfer in reciprocating ribbed channels have been undertaken [16–19]. Indeed, no previous researchers have investigated heat transfer in the antigravity reciprocating open thermosyphon with rib-roughened walls.

The unsteadiness of the reciprocating forces have been shown to have considerable effect on the dynamic structures of vortices and secondary flows induced in channels fitted with ribs , and these effects may improve or impede heat transfer [18,19]. The effect of ribs on duct flow heat transfer depends on the external force field present and on the geometric nature of the ribs themselves [13–22]. Thus, the lack of fundamental knowledge concerning the performance of this particular cooling geometry, despite its apparent engineering application, has been the motivation for the present investigation. The present paper describes the results of a series of experiments aimed at studying the effect of reciprocation on heat transfer in a square-sectioned antigravity open thermosyphon with two opposite walls roughened by the use of staggered transverse ribs. The direction of the reciprocation is along the central axis of the open thermosyphon tube.

Initially, the heat-transfer performance of the static antigravity open thermosyphon was investigated. In this way, a benchmark database was established with which to compare the effect of the thermosyphon reciprocation. The following phase of study involved a systematic investigation of the combined effect of the gravitational free convection with the system reciprocation. The range of experimental parameters covered was typical of those encountered in the real engine case. Thus, the interactive effect of the buoyancy due to the Earth's gravity and the effective body force created by the reciprocation, together with a transient inertial force due to reciprocation, has been revealed.

Experimental Strategy

Figure 2 illustrates the simplified geometric flow system being studied to simulate the piston shaker-cooling concept. The

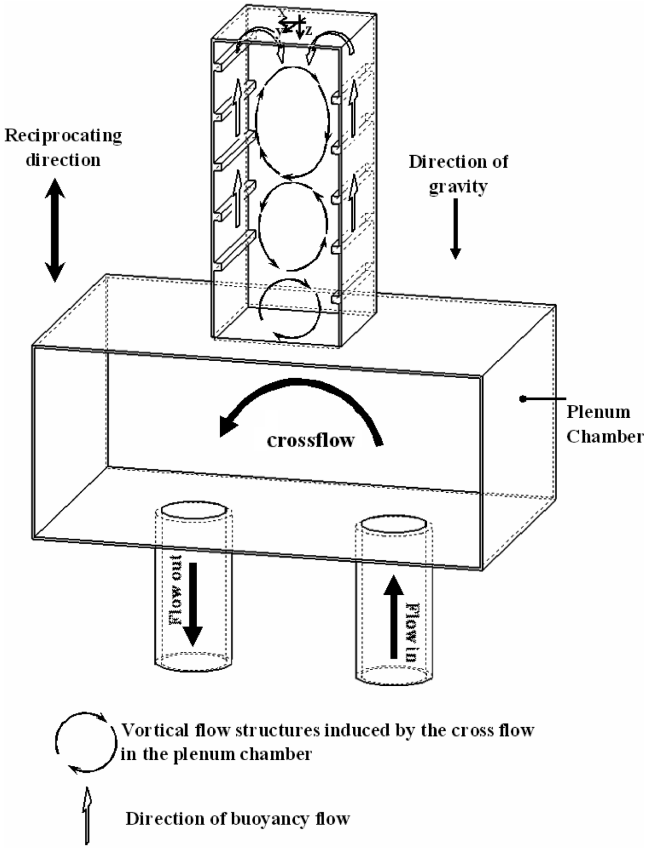

Fig. 2 Simplified geometric flow system in an antigravity open thermosyphon with two opposite rib floors.

thermosyphon tube and the fluid reservoir reciprocate and coolant flows into and out of the reservoir, as illustrated in the figure. The thermosyphon tube is square in cross section, with two opposite walls rib-roughened, as shown. The two ribbed walls are uniformly heated, and the two opposite walls are adiabatic. The vortical cell triggered by the crossflow in the fluid reservoir induces a counter-rotating vortex, after which the vortices are sequentially induced along the thermosyphon tube. These vortical cells construct the main flow structure in the thermosyphon tube, which leads the dependency of cooling performance on the geometries of reservoir and thermosyphon tube. When heat fluxes are supplied from two opposite rib floors, the heated coolant generates surface flows, either driven by the Earth's gravity or by the reciprocating acceleration, toward the blind end of the thermosyphon tube. Surface ribs periodically perturb the inward buoyancy flows, which affects the vortices and boundary layers in the thermosyphon tube. The presence of buoyancy flow adds the additional complexities for the fluid flow and heat-transfer process, in particular, for the flow region adjacent to the blind end of the thermosyphon tube. Nondimensional groups that describe these physical processes present in this flow/heat-transfer system may be derived as follows.

The oscillatory motion produced by the engine piston is not truly sinusoidal and depends on the ratio of the connecting rod length to the crankshaft. When this ratio is greater than eight, the reciprocating motion is well approximated as a simple harmonic in nature [23]. In this case, the oscillatory motion of the flow system may be described as

$$z = a\sin(\omega t) \tag{1}$$

Consider the Cartesian coordinate reference frame shown in Fig. 2. The origin of the frame oscillates and the fluid velocity components relative to this origin are u, v, and w in the coordinate directions x, y, and z, respectively. The z-direction momentum conservation equation for a fluid having constant properties may be written as

$$\rho_0\left(\frac{\partial w}{\partial t} + u\frac{\partial w}{\partial x} + v\frac{\partial w}{\partial y} + w\frac{\partial w}{\partial z}\right) = -\nabla p + \mu_0\nabla^2 w - \rho_0[g + a\omega^2\cos(\omega t)] \tag{2}$$

where t is time, ρ_0 is the fluid density, and μ_0 is the fluid viscosity. The fluid density and viscosity are evaluated at a reference temperature T_0.

For the case of constant property flow, the effect of the reciprocation may be considered as an effective body force (i.e., an artificial time-dependent gravity). Thus, for the case of zero flow, the pressure generated inside the system will be a modified gravitationally induced hydrostatic pressure p_0, given by

$$\frac{\partial p_0}{\partial z} = -\rho_0[g + a\omega^2\sin(\omega t)] \tag{3}$$

If the fluid has a temperature-sensitive density, heating of the fluid will create buoyancy forces via the Earth's gravity and the reciprocating effective body force. The density of the fluid at any temperature may be linked to the reference density via an equation of the form

$$\rho = \rho_0[1 - \beta_0(T - T_0)] \tag{4}$$

where β_0 is the coefficient of cubical expansion.

Insertion of Eq. (4) into Eq. (2) and introducing the Boussinesq approximation yields

$$\left(\frac{\partial w}{\partial t} + u\frac{\partial w}{\partial x} + v\frac{\partial w}{\partial y} + w\frac{\partial w}{\partial z}\right) = -\frac{1}{\rho_0}\nabla p' + \nu_0\nabla^2 v - \beta_0(T - T_0)[g + a\omega^2\sin(\omega t)] \tag{5}$$

where p' is the algebraic difference between the true pressure and the hydrostatic pressure specified by Eq. (2).

The conservation of energy equation is

$$\frac{\partial T}{\partial t} + u\frac{\partial T}{\partial x} + v\frac{\partial T}{\partial y} + w\frac{\partial T}{\partial z} = \frac{k_0}{\rho_0 C_{p,0}}\nabla^2 T \tag{6}$$

where k_0 and $C_{p,0}$ refer to the thermal conductivity and the constant pressure specific heat of the fluid, respectively, also evaluated at the reference temperature.

The nondimensional groups that parametrically govern the flow and temperature fields may be determined using the following transformations of the dependent and independent variables.

$$X = \frac{x}{d}, \qquad Y = \frac{y}{d}, \qquad Z = \frac{z}{d} \tag{7}$$

$$U = \frac{u}{w_m}, \qquad V = \frac{v}{w_m}, \qquad W = \frac{w}{w_m} \tag{8}$$

$$\chi = \frac{p'}{\rho_0 w_m^2}, \qquad \eta = \frac{(T - T_0)}{\Delta T_f}, \qquad \tau = \omega t \tag{9}$$

In Eqs. (8) and (9), d is a characteristic system length, conveniently taken to the hydraulic diameter of the square-sectioned thermosyphon tube, and w_m is a characteristic fluid velocity, defined as

$$w_m = \dot{m}/(\rho_0 d^2) \tag{10}$$

where $\dot{m}$ is the coolant flow rate passing through the reservoir, and ΔT_f is the temperature rise of the fluid passing through the reservoir, given by

$$\Delta T_f = Q/(\dot{m}C_{p,0}) \tag{11}$$

where Q is the heating power transferred through the surface of the thermosyphon tube, taken to be uniform.

If the transformations given in Eqs. (7–9) are inserted into Eqs. (5) and (6), we get, after some routine algebraic manipulation, the following parametric form of the axial momentum conservation equation and the energy equation.

$$Pu\left(\frac{\partial W}{\partial \tau}+U\frac{\partial W}{\partial X}+V\frac{\partial W}{\partial Y}+w\frac{\partial W}{\partial Z}\right)=-\frac{\partial \chi}{\partial Z}+\frac{1}{Re}\nabla^2 W + \frac{Gr_g+Gr_p\sin(\tau)}{Re^2} \tag{12}$$

$$Pu\frac{\partial \eta}{\partial \tau}+U\frac{\partial \eta}{\partial X}+V\frac{\partial \eta}{\partial Y}+W\frac{\partial \eta}{\partial Z}=\frac{1}{RePr}\nabla^2\eta \tag{13}$$

where

$$Re=\frac{\rho_0 w_m d}{\mu_0} \tag{14}$$

$$Pu=\frac{\omega d}{w_m} \tag{15}$$

$$Gr_g=\frac{g\beta_0 d^3\Delta T_f}{\nu_0^2} \tag{16}$$

$$Gr_p=\frac{a\omega^2\beta_0 d^3\Delta T_f}{\nu_0^2} \tag{17}$$

$$Pr=\frac{\mu C_{p,0}}{k_{f,0}} \tag{18}$$

The nondimensional parameters given by Eqs. (14–18) govern the heat transfer and flow in this system. The Reynolds number may be interpreted as the ratio of fluid inertial forces to viscous forces in the usual manner. The pulsating number has its origin in the transient term of the total derivative of the momentum equation and expresses the ratio of the transient inertial forces, induced by the reciprocation, to the fluid inertial force. The gravitational Grashof number expresses the ratio of the buoyancy forces due to the Earth's gravitational field to viscous forces. The reciprocating Grashof number expresses the ratio of the buoyancy forces due to the effective body force field created by the reciprocation to viscous forces. The Prandtl number characterizes the fluid in the usual manner.

Because the fluid velocities U, V, and W are interrelated in the convective term of the momentum equation, the variation in axial velocity W, due to reciprocation, also affects the velocities of U and V. The preceding argument suggests that the nondimensional fluid velocities U, V, and W and the nondimensional fluid temperature may be expressed as

$$U,V,W=U,V,W(X,Y,Z,Re,Pu,Gr_g,Gr_p,Pr) \tag{19}$$

$$\eta=\eta(X,Y,Z,Re,Pu,Gr_g,Gr_p,Pr) \tag{20}$$

The solutions of Eqs. (19) and (20) are also subject to the hydrodynamic, thermal, and geometric boundary conditions at the interface between the solid wall and the coolant flow. These boundary conditions include the specific internal geometries of the duct selected (i.e., the cross-sectional shape and length of the thermosyphon tube, together with a full geometric description of the rib geometry and the plenum chamber geometry).

The variation of the Prandtl number for air is small over the range of temperature covered by the experimental program undertaken. Therefore, the influence of the Prandtl number may be conveniently removed from Eqs. (18) and (19).

Based on the physical argument described previously, the experimental program was designed to permit the z-wise temperature distribution along the two heated walls of the thermosyphon tube to be examined over a range of flow and reciprocation conditions. These measurements were made on the centerline of the two heated walls at rib and midrib locations.

Additionally, at these z-wise locations, thermocouples were inserted into the flow to give some indication of the fluid-temperature response to flow and reciprocation. To minimize the flow disturbance caused by these thermocouples, the sensing bead of the thermocouples was located near to the adiabatic walls of the thermosyphon tube and on the centerline of these surfaces. Full dimensional details are given in the next section.

Thus, for a given geometrical configuration, the measured nondimensional wall temperature $\eta_w(Z)$ and the nondimensional fluid temperature $\eta_f(Z)$ are expected to be functionally related to the Reynolds number, the pulsating number, the gravitational Grashof number, and the reciprocating Grashof number in some manner.

With convective heat transfer, it is customary to link the heat transfer from a surface to the motivating temperature difference using the concept of a heat-transfer coefficient or its nondimensional counterpart, the Nusselt number. For the present series of exploratory experiments, a local heat-transfer coefficient was defined, based on the measured wall- and fluid-temperature difference at a particular z-wise location, as

$$h(z)=\frac{q(z)}{[T_w(z)-T_f(z)]} \tag{21}$$

where q is the heat flux at some z-wise location on the heated walls. The corresponding local Nusselt number $Nu(z)$ becomes

$$Nu(z)=\frac{h(z)d}{k_0} \tag{22}$$

Some routine algebra permits the local Nusselt number to be expressed in terms of the nondimensional wall and fluid temperature, as

$$Nu(Z)=\frac{RePr}{[\eta_w(Z)-\eta_f(Z)]}\frac{d^2}{A_s}=\varphi[Z,Re,Pu,Gr_g,Gr_p] \tag{23}$$

where φ is some functional relationship between the relevant nondimensional numbers.

As mentioned earlier, the strategic aim of the present study is to identify the individual and combined effects of the nondimensional groups shown in Eq. (23). Note that as the temperature difference between the wall and the fluid approaches zero, the effect of buoyancy also diminishes. Thus, in the limiting case of zero buoyancy, Eq. (23) must asymptote toward the form

$$Nu(Z)=\varphi_{ZB}[Z,Re,Pu] \tag{24}$$

where φ_{ZB} is the zero-buoyancy relationship.

The experimental program described next involved a systematic variation of the controlling nondimensional groups, to attempt to reveal the functional form of Eqs. (22) and (23). Details of the experimental apparatus now follow.

Experimental Apparatus

A brief description of the reciprocating facility and a detailed description of the test geometry are now presented. Figure 3 shows a schematic drawing of the reciprocating facility, which has been previously reported [1,18]. As shown, cooling air fed from a compressor unit (1) was directed into the heat-transfer test module (2) through two control valves (3 and 4), a float-type volume flow

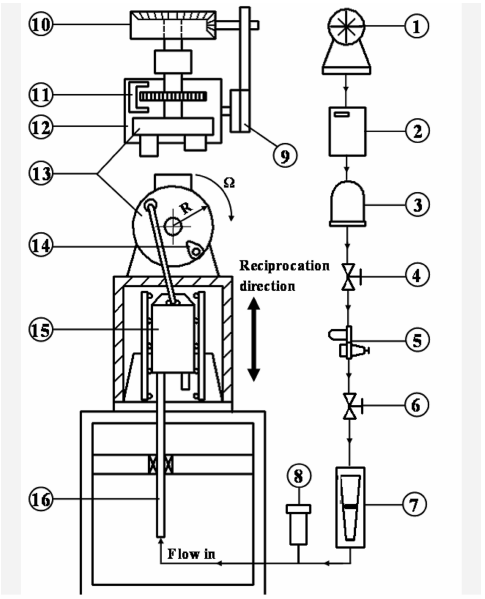

(1) Compressor
(2) Dehumidifier
(3) Air tank
(4) Stop valve
(5) Pressure regulator and filter
(6) Needle valve
(7) Flow meter
(8) Pressure gauge
(9) Pulley-belt unit
(10) Gear box
(11) Optical pick-up
(12) Electrical motor
(13) Fly wheel
(14) Balance weight
(15) Heat transfer test module
(16) Flow calming tube

Fig. 3 Schematic diagram of the reciprocating facility.

meter (5), a digital pressure gauge (6), and a flow-calming tube (7). A thermocouple, which penetrated into the pipeline after the flow meter (5), measured the flow temperature for the evaluation of coolant mass flow rate. Adjustment of the needle valve (4) determined the flow rate required to achieve the predefined Reynolds number value. The coolant was vented through the exit pipe of the heated test module after it passed through the heated test section. The reciprocating motion of the test module (2) was created by a crank-wheel mechanism driven by a 1500-W dc electrical motor (8). Using the pulley-belt unit (9) and the gear box (10), the flywheel (11) could be controlled to a desired rotational speed. A counterbalance weight (12) was fixed on the rotating wheel (10) to maintain dynamic balance during the reciprocating tests. An optical encoder (13) was installed on the shaft to measure the rotational speed for the evaluations of pulsating number and reciprocating Grashof number.

Figure 4 shows the constructional details of the square-sectioned antigravity open thermosyphon that was actually tested. As shown, five transverse ribs were arranged in a staggered manner along each side of the two opposite walls. These two ribbed surfaces and the sealed-end heating surface were made of a continuous 15-mm-wide, 0.1-mm-thick stainless-steel foil (1). This ribbed heating foil (1) was clamped between four Tufnol sidewalls (2) to secure its position in the thermosyphon. The two ends of the ribbed surfaces were fixed on to the Tufnol bottom wall of the thermosyphon (3), where an electrical supply was connected to directly heat the ribbed stainless-steel walls. A high-current, low-voltage dc electrical power supply was directly fed through the heating foil (1) to generate the uniform flux heating condition. Starting from the center of the top sealed surface (4), twelve K-type thermocouples were welded on the back of the stainless-steel heating foil (1) to measure the wall temperatures at locations corresponding to the rib and midrib positions. Ceramic cement was filled in behind each rib after the wall thermocouples were positioned. At the ductwise locations in which the wall-temperature measurements were made, 12 thermocouples along the centerline of the insulated sidewall (2) penetrated into the flow passage with 1-mm depth to measure the fluid temperature. The 100-

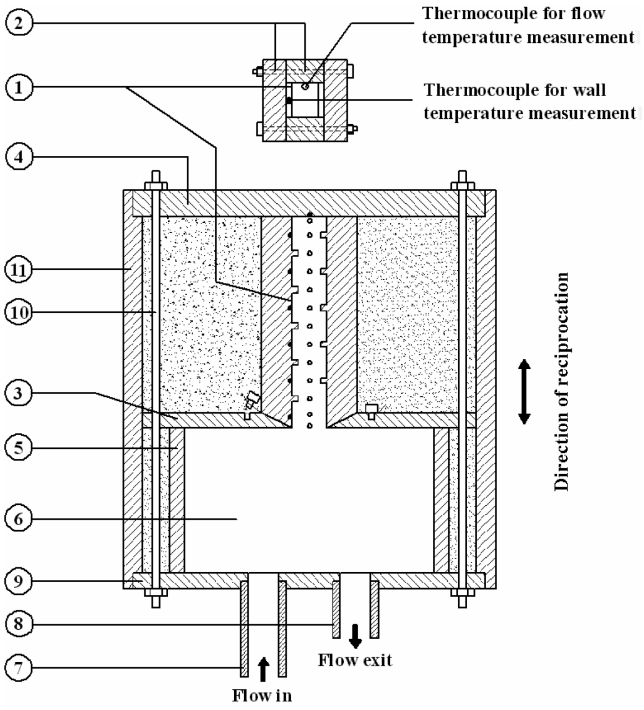

Rib height / hydraulic diameter ratio (e/d) = 0.1
Pitch / rib height ratio (Pi/e) =10
Land / pitch ratio (I/Pi) = 0.1
Aspect ratio of thermosyphon (d/H) = 0.167
Apsect ratio of plenum chamber (Wd/Hp) = 1.33
Blockage ratio of thermosyphon (d/Wd) = 0.25

(1) Heating foil
(2) Tufnol side walls
(3)Tufnol bottom wall
(4) Tufnol top wall
(5) Plenum chamber side wall
(6) Plenum chamber
(7) Flow entrance
(8) Flow exit
(9) Plenum chamber bottom wall
(10) Stiffing tube

Fig. 4 Constructional details of the heat-transfer test module.

mm-wide Tufnol bottom wall (3) with four 50-mm-high Tufnol sidewalls (5) formed a square-sectioned plenum chamber (6). A circular-sectioned coolant entrance tube (7) and an exit tube (8) permitted cooling air to be fed through the reservoir. These tubes were 12-mm in diameter and were flush-fitted to the bottom end of the plenum chamber (9). The centers of the flow entrance and exit tubes (7 and 8) were located 32.5 mm from the inner sidewalls of the plenum chamber (5). Four draw bolts (10) tightened the complete test assembly, which was encapsulated within a stiffening tube (11). An in-fill of the thermal insulation material was packed in the space between the test section and the stiffening tube (11) to minimize external heat loss. The built-up heat-transfer test module was vertically mounted onto the reciprocating facility so that the antigravity open thermosyphon situation was simulated. The length and hydraulic diameter of the test section were 90 mm and 15 mm, respectively. Geometric features of the square, ribbed test section were specified in Table 1.

An electrical power control of heating power provided the required heating current. Adjusting the heating power supply varies the relative strength of the overall buoyancy level at any fixed flow condition. Before undertaking the flow tests, the external heat loss characteristics were determined via a series of heat loss calibration tests. For tests at the highest temperature settings and reciprocating frequency, the estimated heat loss during an experiment was about 19.8% of the total heating power supply.

Table 1 Geometric features of the test section

Geometric feature	*Dimension*, mm
Vertical height of the thermosyphon	90
Hydraulic diameter of the thermosyphon	15
Rib height	1.5
Rib land	1.5
Ribs pitch	15
Height of the plenum chamber	50
Width of the plenum chamber	100
Geometrical dimensionless groups	*Dimensionless ratio*
Aspect ratio of the thermosyphon (d/H)	0.167
Aspect ratio of the plenum chamber (Wd/Hp)	2
Blockage ratio of the thermosyphon (d/Wd)	0.15
Rib-height/hydraulic-diameter ratio (e/d)	0.1
Pitch/rib-height ratio (Pi/e)	10
Land/pitch ratio (l/Pi)	0.1

All of the temperature measurements were monitored and stored in a DX33 PC using a Trend-Link Fluke Hydra 2620A-100 data logger for the subsequent data processing.

Data Reduction and Experimental Program

The local convective heat flux (used for calculating the nondimensional wall and fluid-temperature) and the Nusselt number distribution were obtained by subtracting the external heat loss from the total heating power. The heat loss was evaluated based on the results from a series of heat loss calibration runs. The local coolant thermal and transport properties (i.e., density, constant pressure specific heat, thermal conductivity, and viscosity) were evaluated by means of standard polynomial curve-fitting functions using the measured local fluid temperature as the argument.

Because the viscosity and density of the coolant varied with the temperature, the mass flow rate was adjusted to limit variations of the Reynolds and pulsating numbers (at the entrance of the thermosyphon tube) to within $\pm 1\%$ of the nominal values selected.

Initially, the instrumentation and data reduction program were analyzed with a series of static baseline heat-transfer experiments. Correlations of the local heat transfer, in terms of the Reynolds number and gravitational Grashof number, were determined for this static benchmark phase. This phase was followed by a series of reciprocating experiments. The reciprocating data were produced at fixed Reynolds numbers. At each selected Reynolds number, five sets of tests at the reciprocating frequencies of 0.83, 1.25, 1.67, 1.83, and 2 Hz were performed. The data generated in this manner revealed the effect of reciprocation on heat transfer. At each selected Re-Pu combination, five different levels of heating power [which raised the wall temperature at the sealed end of the thermosyphon tube to nominal levels of 50, 75, 100, 110, and 120 (130)°C, respectively], were used to systematically vary the effect of buoyancy by creating a range of gravitational and reciprocating Grashof numbers.

The online data acquisition system collected and stored the instantaneous temperature measurements for every period of 10 s. These measurements were subsequently time-averaged and scanned. A quasi steady-state condition was assumed when the variations of the time-averaged wall temperatures remained within ± 0.3°C. A period of about 45 min was required to achieve a steady-state condition. The range of nondimensional parameters covered is given in Table 2.

An analysis of the experimental errors for this apparatus was undertaken [24]. The measured wall-to-fluid temperature difference was in the range of 8–43°C. In this range, it was estimated that the maximum uncertainty in the determination of Nu, Re, Pu, Gr_g, and Gr_p were 15, 7, 2.5, 6.6, and 7.3%, respectively.

Table 2 Range of experimental nondimensional parameters

Nondimensional parameter	Range
Reynolds number	1200–4100
Pulsating number	0–0.08
Gravitational Grashof number	270–1500
Reciprocating Grashof number	230–5800

Results and Discussion

Static Results

In the absence of reciprocation, Eq. (20) shows that the local heat transfer in the static antigravity open thermosyphon is dependent on the Reynolds number and Gr_g alone.

Figure 5 typifies the Z-wise wall- and fluid-temperature distributions obtained with two different heating powers at Reynolds numbers of 2100 and 3900, respectively. Referring to Figs. 5a and 5c, which plot raw temperature data, we note that the region of highest temperature occurs near the sealed end of the thermosyphon tube ($0 < Z < 3.5$). There is a tendency for the wall temperature to zigzag in a sawtooth manner in this region, with the temperature peaks occurring at the rib locations. The antigravity nature of this stationary thermosyphon appears to suppress convective movement of the fluid, with a tendency for the coolant to stratify within this region of high temperature. In an enclosure with wavy sidewalls, buoyancy force has been found to induce small-scale vortical cells along the wavy surface. This tends to improve heat transfer from the levels found in a smooth-walled enclosure [25]. It is therefore felt that the development of the Z-wise zigzag wall-temperature variation in this hot region ($0 < Z < 3.5$) is due to the small-scale vortical circulations induced over the ribbed surfaces by the gravitational buoyancy force.

In the region $Z > 4$, as depicted in Figs. 5a and 5c, a rapid Z-wise reduction in wall temperatures occurs and the zigzag pattern is considerably suppressed. This wall-temperature reduction is caused by the penetration of coolant into the thermosyphon tube from the

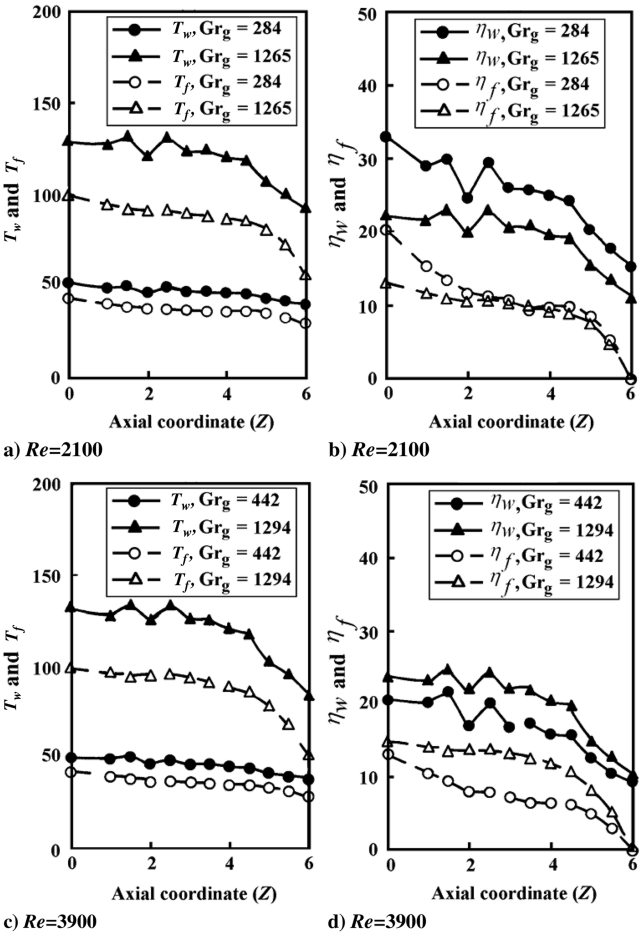

Fig. 5 Axial wall- *and* fluid-temperature distributions in a static thermosyphon.

plenum chamber [4]. Although it adjusts inside the entrance to produce a natural boundary between an upward and downward movement of flow. It is this induced circulation of fluid that effectively transports the heat transfer from the tube surface.

The measured fluid temperature showed no tendency to zigzag in the Z-wise direction, as typified by Fig. 5. There was a continuous reduction in fluid temperature as the open end of the thermosyphon tube was approached. Indeed, the fluid temperature falls off rapidly in the vicinity of the tube entrance, particularly at the higher levels of Gr_g.

The effect of gravitational buoyancy and the penetration of flow at the inlet plane on the nondimensional wall and fluid temperature are shown in Figs. 5b and 5d, respectively, for the two Reynolds numbers cited. Note that for convenience, the reference temperature used in the definition of the nondimensional temperature has been taken to be the measured fluid temperature at the entry plane of the thermosyphon tube. This means that the nondimensional fluid temperature becomes zero at the inlet to the thermosyphon tube for all tests. Figures 5b and 5d again show the significant effect of Gr_g on the temperature field. At a Reynolds number of 2100, the difference in the nondimensional wall temperatures at a given axial location tends to reduce as the Z value increases. This suggests that the effect of buoyancy is becoming less important in the entry region of the thermosyphon and this is consistent with the domination of the induced flow circulation from the reservoir. At the higher Reynolds number value of 3900, this feature is even more pronounced, as shown in Fig. 5d. A tendency for the nondimensional fluid temperature to converge is also evident in the near entry region.

The main observations that may be made from the results shown in Fig. 5 are that the movement of fluid through the reservoir induces a flow circulation in the entry region of the thermosyphon tube and that the penetration of this circulation deepens with increases in the Reynolds number. Thus, the local wall-to-fluid heat transfer will be very much influenced by this induced circulation in the vicinity of the tube entrance. Additionally, there is a clear superimposed effect of buoyancy, as characterized by the gravitational Grashof number. Local heat transfer is significantly increased by buoyancy, particularly in the vicinity of the sealed end of the thermosyphon tube, because the values of $\eta_w - \eta_f$ decrease when the gravitational Grashof number increases. Detailed descriptions of the gravitational buoyancy effect will be presented later.

It is clearly shown in Fig. 5b that at the lower level of Reynolds number (2100), the two nondimensional wall-temperature curves remain separated along the entire tube length. This suggests that both mechanisms (induced entry flow and buoyancy) are important at this lower Reynolds number. In evidence of fluid migrating into the open-ended region of the thermosyphon tube, there can be no net flow at any one cross-sectional plane, because the end is sealed. This means that the flowfield must persist through several large-scale three-dimensional vortices so that the zero net flow through each cross-sectional plane of the thermosyphon tube can be preserved. For the higher level of Reynolds number (3900), the improved convergence of the two nondimensional wall-temperature curves for $Z > 2$ in Fig. 5d suggests that local heat transfer in this region is dominated by the induced circulation from the reservoir. In the region of $0 < Z < 2$, buoyancy is influencing the wall-temperature response, as indicated by the separation of the two lines.

Local Nusselt numbers were calculated, as defined by Eq. (21), at each measurement station. Figure 6 shows the typical axial variations of local Nusselt number Nu_0 for two Reynolds number values (2100 and 3900). Three heater settings were used for each Reynolds number, giving three levels for the gravitational Grashof number. As shown in Fig. 6a, the increases of the gravitational Grashof number from 284 to 1265 consistently increase the local Nusselt number all over the rib-roughened surface. Buoyancy effects are again seen to prevail over the entire thermosyphon tube for a Reynolds number of 2100. The regular zigzag pattern of Nusselt numbers that consistently show higher Nusselt numbers at the midrib locations are observed in the region of $1 < Z < 4$ for all of the gravitational Grashof numbers tested. This is consistent with the nondimensional temperature data shown in Fig. 5. As the flow region approaches the open end of the thermosyphon, the regular zigzag pattern is gradually diminished and a Z-wise increase of Nusselt numbers appears from $Z = 3.5$. The axial increase of Nusselt number for $Z > 3.5$, shown in Fig. 6a, demonstrates the effect of coolant penetration, which is Reynolds-number-dependent for a given flow geometry, as argued earlier. Significant coupling effects linking the Reynolds and Grashof numbers on heat transfer are thus expected in this flow region.

When the Reynolds number increases from 2100 to 3900, the Z-wise increase of Nusselt number tends to start from $Z = 1.5$. The regular zigzag Nusselt number variation still prevails over the region of $1 < Z < 4$ for all of the gravitational Grashof numbers tested, as shown in Fig. 6b. As with the data shown in Fig. 5, there is a tendency for the Nusselt number variation in the region of $Z > 4$, for a Reynolds number of 3900, to be more tightly banded. Again, this is due to the induced flow from the reservoir becoming more dominant in comparison with the influence of buoyancy.

The preceding discussion demonstrated that two interacting flow mechanisms control the heat-transfer characteristics of this form of closed antigravity thermosyphon. First, flow induced into the entry section of the thermosyphon tube occurs, due to the continuous circulation of fluid through the reservoir. Second, the temperature-dependent fluid density combines with the gravitational force to produce a free-convection effect. An attempt was made to determine a correlating equation for Nu_0, in terms of the relevant nondimensional parameters discussed in Sec. . The structure of this correlating equation has to be mathematically consistent with the controlling physics.

In the limiting case of zero buoyancy, the heat-transfer mechanism is entirely controlled by the induced flow from the reservoir. For the static thermosyphon, therefore, Eq. (24) reduces to

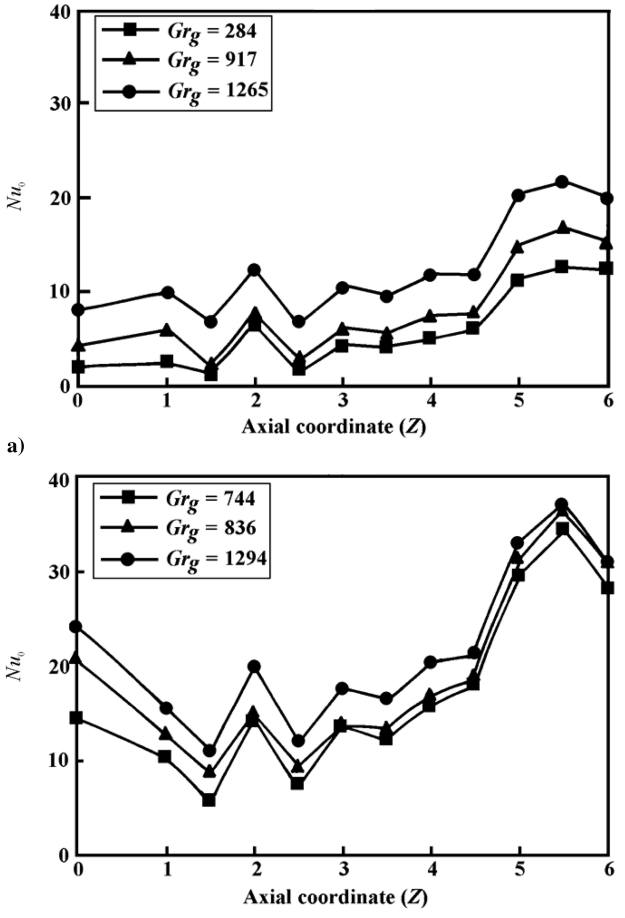

Fig. 6 Typical axial variations of the local Nusselt number in a static thermosyphon at a) $Re = 2100$ and b) $Re = 3900$.

$$Nu_{0,ZB} = \alpha(Z, Re) \tag{25}$$

where $Nu_{0,ZB}$ is the zero-buoyancy asymptotic Nusselt number and α is an, as yet, undetermined function of the axial location along the tube and the Reynolds number.

Figure 7 shows a series of graphs illustrating the variation of local Nusselt number with gravitational Grashof number for the three Reynolds numbers tested. At each measuring station, the local Nusselt number increases with increasing gravitational Grashof number. These individual curves were numerically extrapolated back to the origin to determine the zero-buoyancy Nusselt number $Nu_{0,ZB}$ for each axial location at which measurements were made. The variation of the zero-buoyancy Nusselt number with Reynolds number at each measurement location is also shown in Fig. 7. These individual curves were correlated using an exponential form, and the results for each axial location are given in Table 3.

At the center of the sealed top end of the tube ($Z = 0$), the largest increasing rate of Nusselt number with increasing gravitational Grashof number is found. Buoyancy effects are most effective at this spot in the static thermosyphon. For all of the axial locations, the increasing rate of Nusselt number with gravitational Grashof number reduces when the Reynolds number increases. This result reflects the weakened buoyancy effects, as demonstrated previously. Clearly, the values of a zero-buoyancy asymptotic Nusselt number, defined in each plot shown in Fig. 7, increase with Reynolds number and are Z-location-dependent.

Table 3 Functions of α and γ in heat-transfer correlations for Nu_0

Z	$Nu_{0,ZB} = \alpha\{Re, Z\}$	$\gamma\{Re, Z\}$	Location
0	$2.15E\text{-}8 \times Re^{2.47}$	$1.513E\text{-}4e^{(3.335-6.048E-4\times Re)}$	Central spot (top end)
1	$8.033\text{-}7 \times Re^{2.27}$	$1.536E\text{-}4e^{(3.061-6.422E-4\times Re)}$	Midrib location
1.5	$3.182E\text{-}8 \times Re^{2.312}$	$7.921E\text{-}5e^{(3.513-4.6E-4\times Re)}$	Rib location
2	$4.906E\text{-}5 \times Re^{1.52}$	$9.491E\text{-}5e^{(3-5.514E-4\times Re)}$	Midrib location
2.5	$2.297E\text{-}9 \times Re^{2.668}$	$1.16E\text{-}4e^{(3.471-6.588E-4\times Re)}$	Rib location
3	$7.411E\text{-}6 \times Re^{1.746}$	$1.063E\text{-}4e^{(3.001-6.347E-4\times Re)}$	Midrib location
3.5	$1.321E\text{-}5 \times Re^{1.668}$	$9.248E\text{-}5e^{(3.001-6.081E-4\times Re)}$	Rib location
4	$3.072E\text{-}5 \times Re^{1.589}$	$7.74E\text{-}5e^{(3.062-5.551E-4\times Re)}$	Midrib location
4.5	$2.937E\text{-}5 \times Re^{1.322}$	$8.624E\text{-}5e^{(3.001-7.099E-4\times Re)}$	Rib location
5	$5.118E\text{-}4 \times Re^{1.322}$	$5.788E\text{-}5e^{(3-5.862E-4\times Re)}$	Midrib location
5.5	$7.05E\text{-}4 \times Re^{1.296}$	$6.577E\text{-}5e^{(2.919-6.462E-4\times Re)}$	Rib location
6	$3.331E\text{-}3 \times Re^{1.093}$	$5.988E\text{-}5e^{(2.8-6.441E-4\times Re)}$	Midrib location

At the limiting case, when the Reynolds number is zero, the extrapolated zero-buoyancy asymptotic Nusselt number values obtained at all of the Z locations also converge to zero. However, the concept of the present form of the thermosyphon (i.e., fitted with a

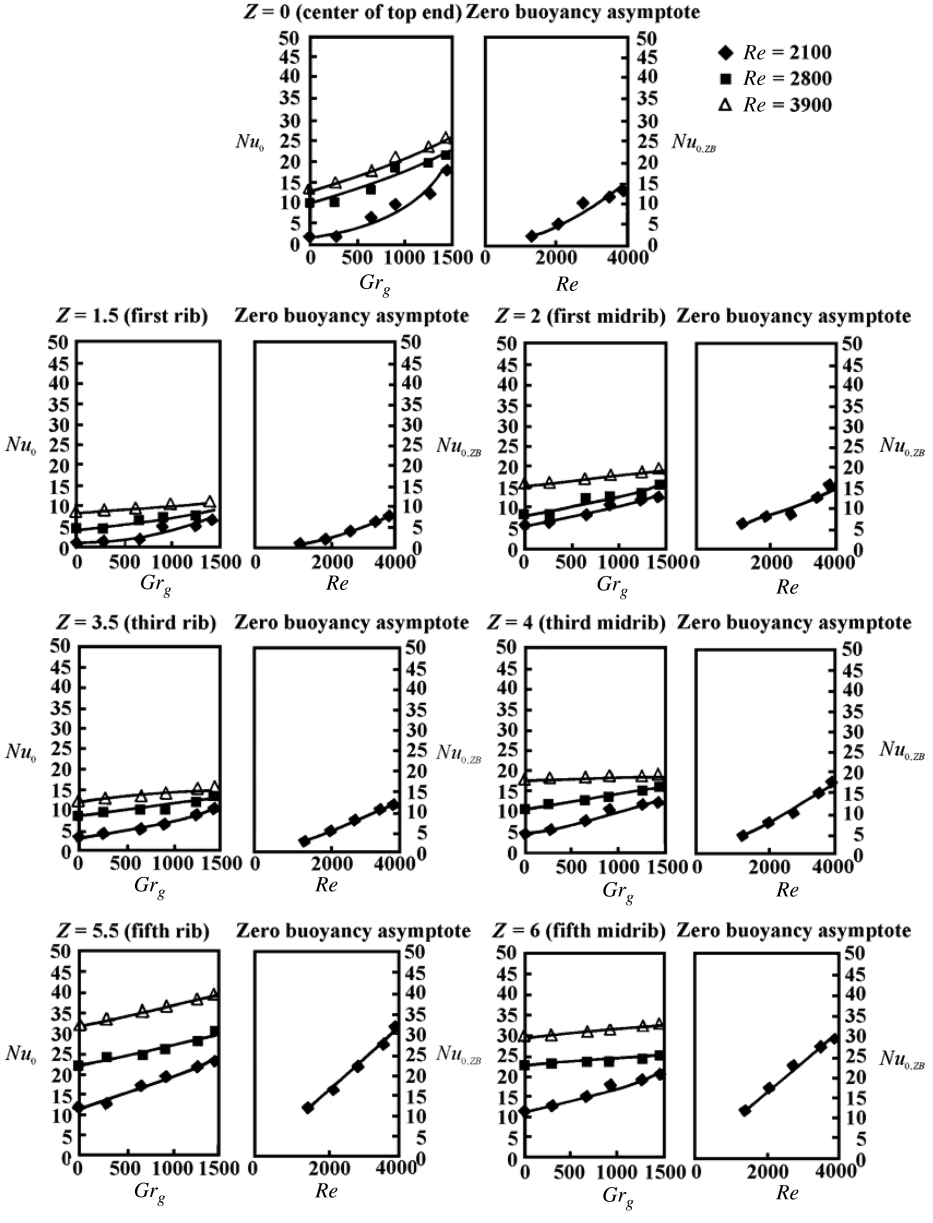

Fig. 7 Variations of local Nusselt number with gravitational Grashof number at different Reynolds numbers in a static thermosyphon.

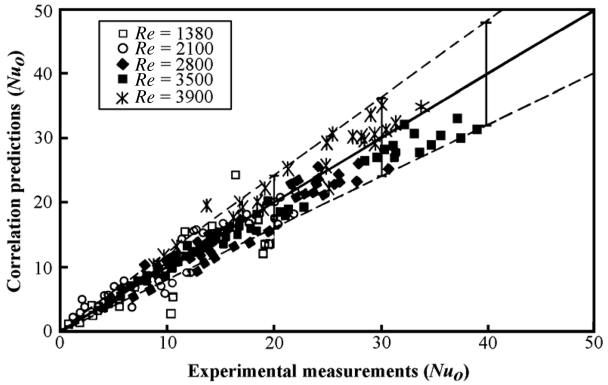

Fig. 8 Comparison of actual measurements of Nu_0 with correlation results.

reservoir through which a constant flow occurs) is invalid when the flow is zero. In this case, the system cannot achieve a steady-state condition. A detailed study of the data led to the proposal that the combined effect of Reynolds number and gravitational Grashof number may be correlated with an equation having the following mathematical structure.

$$Nu_0 = Nu_{ZB} \exp\{\gamma(Z, Re) Gr_g\} \tag{26}$$

where Nu_0 is the local Nusselt number for the static condition and γ is an, as yet, unspecified function that allows for the effect of gravitational buoyancy. The structure of Eq. (26) ensures that the Nusselt number approaches its zero-buoyancy limiting case as the gravitational Grashof number approaches zero.

A detailed examination of the local data gave rise to the proposals shown in Table 3 for the γ function. Figure 8 compares the actual measured experimental local Nusselt numbers with those predicted using the empirical correlations given in Table 3. All α functions collected in Table 3 vanished as $Re = 0$. Equation (26) satisfies both limiting conditions $Gr_g = 0$ and $Re = 0$. Over the parametric range studied for Nu_0, the discrepancies between the correlation and experimental results for 95% of the entire set of Nu_0 data are controlled within $\pm 20\%$. Equation is treated as the heat-transfer reference with zero reciprocation. Because of the runaway nature of the exponential function, the correlations given in Table 3 should be restricted to the range of experimental parameters covered by the present investigation. These correlations will be used in the next subsection to evaluate the additional effects created by reciprocation of the thermosyphon.

Reciprocating Results

Convections of fluid momentum and energy in a reciprocation system are Pu-dependent and are subject to buoyancy interactions motivated by reciprocating forces, as described in Eqs. (12) and (13). Flow pulsations and oscillating pressure waves are generated within a reciprocating thermosyphon, which influences the vortical flow structure, the coolant penetration, and the buoyancy-induced wall flows over the rib floors. This produces attendant temporal heat-transfer variations at each measurement station. The present study generates the time-averaged heat-transfer data along the centerlines of two opposite rib floors in the thermosyphon, with the individual and interactive impacts of each controlling flow parameter in Eq. (23) examined.

Influences of reciprocation directly reflect on the distributions of wall and fluid temperature, as shown in Fig. 9, in which the Z-wise distributions of wall and fluid temperatures obtained (with two different heating powers for Reynolds numbers of 2100 and 3900 at the reciprocating frequency of 2 Hz) are displayed. Two pulsating numbers of 0.08 and 0.04 are produced for the test conditions of $Re = 2100$ and 3900, respectively. The comparison of static and reciprocating results depicted in Figs. 5 and 9 highlights the reciprocating impacts. The apparent zigzag T_w variations shown in Figs. 5a and 5c in the static thermosyphon are considerably suppressed in the reciprocating thermosyphon, as seen in Figs. 9a and 9c. The buoyancy-driven wall flows in the static thermosyphon are considerably disturbed by the reciprocating forces. The dominant flow physics for heat transfer in the reciprocating thermosyphon are modified from the static conditions and appear to be pulsating-number-dependent. At the pulsating number of 0.08 ($Re = 2100$ and $F = 2$ Hz), the improved coolant penetration into the reciprocating thermosyphon from the static scenario is demonstrated by the reduced η_f values in the reciprocating thermosyphon, as shown in Fig. 9c from the static reference depicted in Fig. 5c. As a result, the reduced η_f differences between two test results with $Gr_p = 1355$ and 9357 are observed in Fig. 9c. At the pulsating number of 0.04 ($Re = 3900$ and $F = 2$ Hz), the two sets of η_f values in the reciprocating thermosyphon depicted in Fig. 9d are increased from the static counterparts depicted in Fig. 5d, which demonstrates the impeded coolant penetration into the reciprocating thermosyphon at this set of test conditions. Two separate η_f curves obtained with $Gr_p = 1184$ and 4703 are generated in Fig. 9d. Based on the η_f results obtained from Figs. 9c and 9d, the increased and decreased coolant penetrations into the reciprocating thermosyphon take place at the conditions with the higher and lower pulsating numbers, respectively. Inconsistent with the static results, increases of Gr_p values reduced η_w levels, which reconfirms the improving buoyancy effect on heat transfer.

Figure 10 shows the typical axial distributions of local Nusselt number for two sets of Reynolds (pulsating) numbers of 2100 (0.08) and 3900 (0.04) at $F = 2$ Hz. Three heater settings were used for each set of Reynolds and pulsating numbers, giving three values of reciprocating Grashof number. Heat-transfer levels increase from the sealed end toward the entrance of the reciprocating thermosyphon in the axial direction. As shown in Figs. 10a and 10b, the upward data spreads are driven by increasing Gr_p value over the entire reciprocating thermosyphon, with different ranges of data bands at

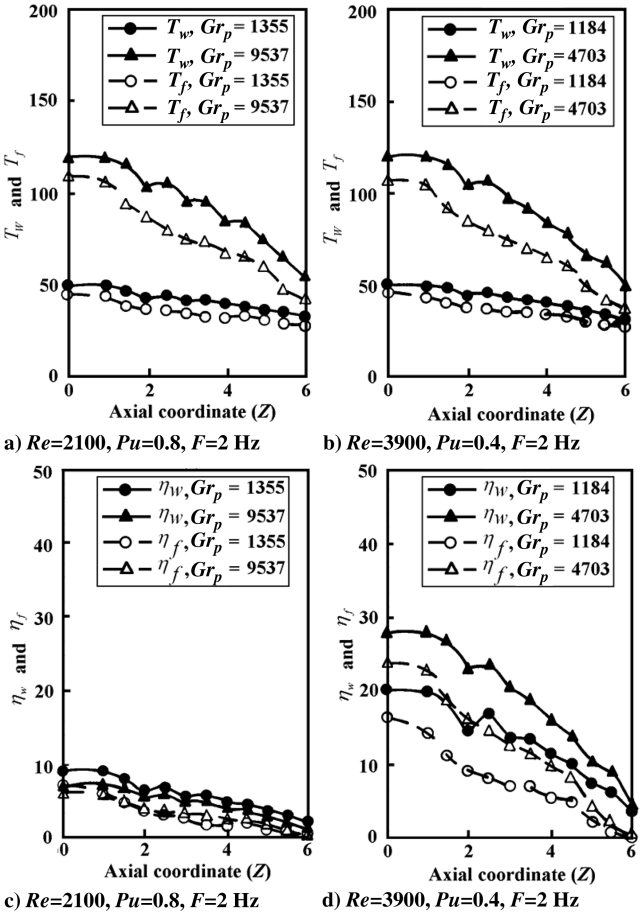

Fig. 9 Axial wall- and fluid-temperature distributions in a reciprocating thermosyphon.

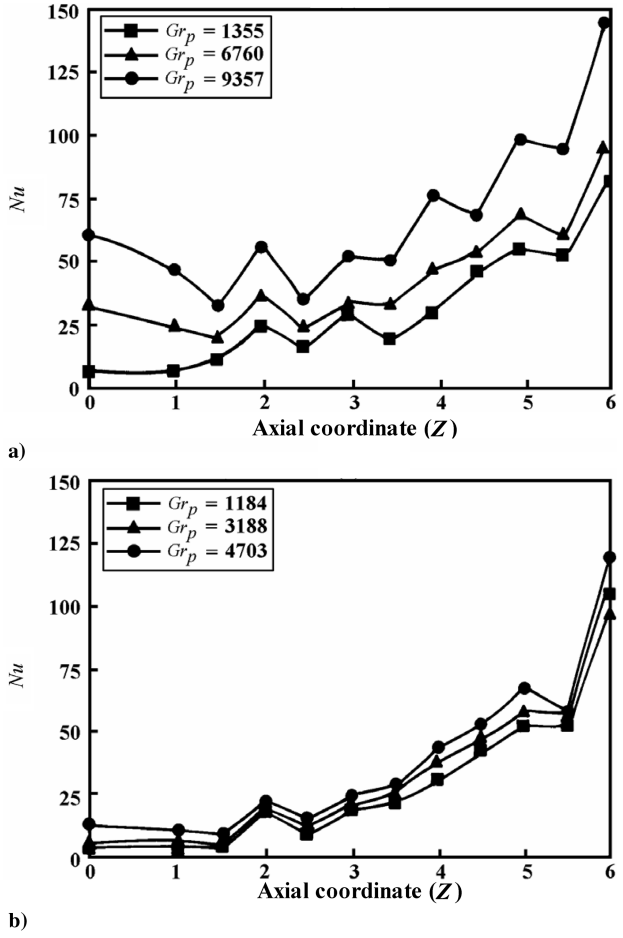

Fig. 10 Typical axial variations of local Nusselt number in a reciprocating thermosyphon at a) $Re = 2100$ and b) $Re = 3900$.

the various measurement spots and for two different test conditions. The reciprocating buoyancy effect improves local heat transfer over the entire reciprocating thermosyphon. The wider data band observed in Fig. 10a indicates the stronger buoyancy effect at the lower Reynolds number of 2100. The enhanced vortical strength in the reciprocating thermosyphon at the higher Reynolds number weakens the buoyancy effect. The various degrees of buoyancy impacts in the reciprocating thermosyphon are intercorrelated with Reynolds and pulsating numbers, which will be further addressed when the data are analyzed parametrically. Nevertheless, the buoyancy effect remains persistent in the reciprocating thermosyphon, with an attendant reduction in its effectiveness as the Reynolds number increases.

It is also worth noting that the Nusselt number at each axial station leveled in Fig. 10a at the Reynolds number of 2100 is generally higher than the Nusselt number value obtained with the higher Reynolds number of 3900, as displayed in Fig. 10b. The increase of Reynolds number from 2100 to 3900 at the fixed reciprocating frequency of 2 Hz reduces the pulsating number from 0.08 to 0.04, which incurs the local heat-transfer impediments in the reciprocating thermosyphon. This trend of heat-transfer reduction in response to the increase of Reynolds number reverses the static results typified in Figs. 6a and 6b. As the reciprocating buoyancy effect with these test conditions improves local heat transfer, the worse heat-transfer scenarios depicted in Fig. 10b are attributed to the pulsating number effect. Heat-transfer variations in the reciprocating thermosyphon from the static references are likely to be interactively linked with the Re, Pu, and Gr_p that formulate the subject of following parametric investigations. To level the heat-transfer variation in the reciprocating thermosyphon from the static reference, the Nusselt number is normalized by the static Nusselt number Nu_0 evaluated from Eq. (26). In this respect, the gravitational Grashof number is also determined using the ΔT_f value acquired from each reciprocating test when Eq. (26) is applied to determine Nu_0. The relative Nusselt number Nu/Nu_0 has to be unity as both Pu and Gr_p approach zero.

Initially, the isolated Gr_p effect at each detected Z station is analyzed by plotting the relative Nusselt number Nu/Nu_0 against Gr_p at constant values of Pu and Re. This is demonstrated by a series of graphs illustrating the variation of local relative Nusselt number Nu/Nu_0 with reciprocating Grashof number for the three pulsating numbers tested at a Reynolds number of 2900, as seen in Fig. 11. At each measuring Z station, Nu/Nu_0 ratios increase as Gr_p increases. Each individual Nu/Nu_0 vs Gr_p curve was numerically extrapolated back to the origin to recover the zero-buoyancy reciprocating Nusselt number ratio $Nu_{ZB}/Nu_{0,ZB}$ at each detected axial station. Justified by the data trends of Nu/Nu_0 vs Gr_p in Fig. 11, which are commonly shared by the entire reciprocating results obtained with all the Reynolds numbers tested, the correlation equation adopted to generate $Nu_{ZB}/Nu_{0,ZB}$ ratios for each Re-Pu combination takes the exponential form of Eq. (27).

$$Nu/Nu_0 = A\{Pu, Re, Z\} \times e^{n\{Pu,Re,Z\}\times Gr_p} \tag{27}$$

With the exponential format, Eq. (27) appears to be the best fit for the entire set of Nu/Nu_0 vs Gr_p curves generated by the present study. Because Eq. (27) is adopted to extrapolate toward the limiting condition of $Gr_p \to 0$ but not used to predict the Nu/Nu_0 ratios with high Gr_p values, the divergent nature of the exponential function for the present application is avoided.

Coefficients A and n in Eq. (27) are functions of Pu, Re, and Z that are, respectively, equal to unity and 0 to satisfy the limiting condition of $Pu \to 0$ and $Gr_p \to 0$ to recover the static heat-transfer reference cited by Eq. (26). The A coefficient and n exponent are, respectively, treated as the $Nu_{ZB}/Nu_{0,ZB}$ ratio and the index that levels the degree of reciprocating buoyancy effect.

Equation (27) enables the ratio of isothermal reciprocating heat-transfer level to the static reference in terms of $Nu_{ZB}/Nu_{0,ZB}$ at the Reynolds number of 2900 to be determined. The Z-wise variations of the series of $Nu_{ZB}/Nu_{0,ZB}$ vs Pu plots displayed in Fig. 11 show the isolated Pu impact on reciprocating heat transfer at the Reynolds number of 2900 with the vanished buoyancy effect. The $Nu_{ZB}/Nu_{0,ZB}$ vs Pu curve collected from each Z station follows a general pattern. Reciprocating heat-transfer levels are initially reduced to be less than the static references and then recovered to show considerable enhancements as Pu increases from 0 to 0.08, except at the central spot on the sealed end ($Z = 0$). At the spot of $Z = 0$, the ratios of $Nu_{ZB}/Nu_{0,ZB}$ at all of the pulsating numbers examined are less than unity, which indicates the heat-transfer impediments from the static condition. With the flow region moving toward the entrance of the thermosyphon, the $Nu_{ZB}/Nu_{0,ZB}$ ratios gradually rise.

The regionally worse heat-transfer scenarios near the sealed end of the reciprocating thermosyphon, in which the buoyant convection dominates the heat-transfer process, are caused by the reciprocation-induced temporal disturbances on the wall flows. Also, the turbulence activities near the sealed end of the thermosyphon are considerably suppressed by nature. Therefore, the interactions of reciprocation with the turbulence in this sealed-end flow region are accordingly diminished, which rules out the possible amplifications of turbulence level by system reciprocation. At the zero-buoyancy conditions, the maximum $Nu_{ZB}/Nu_{0,ZB}$ ratios shown in Fig. 11 reach about four at the pulsating number of 0.08. With buoyancy interactions involved, the synergistic Re-Pu-Gr_p force effects can elevate the relative Nusselt number Nu/Nu_0 to the maximum values of about six. A review of the entire Nu/Nu_0 data generated with all of the Reynolds numbers tested showed that the synergistic Re-Pu-Gr_p effects interacting with the present rib floors produces the Nu/Nu_0 ratios falling in the range of $0.65 \sim 8$. Heat-transfer impediments are observed at the flow conditions, with low Reynolds numbers and low pulsating numbers due to the weakened vortical strengths and coolant penetrations. Such heat-transfer impediments from the static references at the low Reynolds and pulsating numbers draw

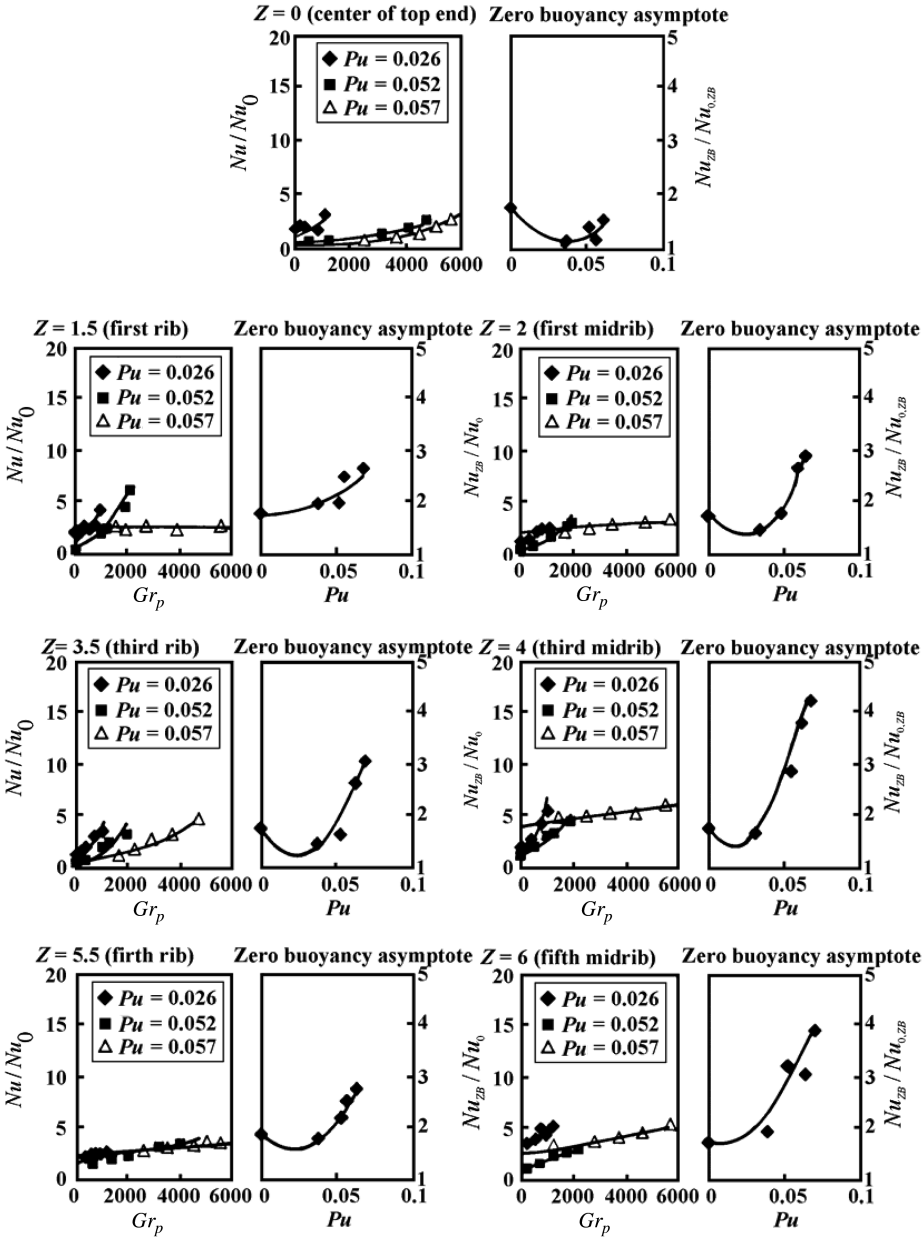

Fig. 11 Variations of local Nusselt number with reciprocating Grashof number at different Reynolds numbers in a reciprocating thermosyphon.

precautions in the design and operating stages for the piston. However, the addition of rib floors on two opposite walls in the reciprocating antigravity open thermosyphon has proven itself with considerable heat-transfer augmentations at high Reynolds numbers and high pulsating numbers. The detailed flow measurements are worthwhile of implementation to clear the heat-transfer physics revealed in Fig. 11.

Heat-transfer results with and without buoyancy interactions, shown in Fig. 11, are obtained at the Reynolds number of 2900. However, as the coolant penetration and the strengths of vortices and vorticity levels in the reciprocating thermosyphon are varied to considerable extents with the Reynolds number, the influences of the pulsating number on the flow mechanisms in this reciprocating thermosyphon are strongly correlated with the Reynolds number. The possible interactive *Re*-*Pu* impacts on heat transfer in the reciprocating thermosyphon are best examined at the isothermal conditions without any buoyancy interaction. The procedure of identifying $Nu_{\mathrm{ZB}}/Nu_{0,\mathrm{ZB}}$ ratios, as illustrated in Fig. 11, is repeated for all of the Reynolds numbers tested. A series of graphs illustrating the variation of $Nu_{\mathrm{ZB}}/Nu_{0,\mathrm{ZB}}$ against Pu at various axial locations for the three Reynolds numbers tested ($Re = 2100$, 2500, and 4100) are collected in Fig. 12. Each data trend revealed in the individual plot of Fig. 12 is forced to be unity at the limiting condition of zero reciprocation ($Pu = 0$), which recasts the static isothermal heat-transfer solution $Nu_{0,\mathrm{ZB}}$. As depicted in Fig. 12, the curve of the $Nu_{\mathrm{ZB}}/Nu_{0,\mathrm{ZB}}$ ratio with initial heat-transfer impediments followed by a subsequent heat-transfer recovery as Pu increases is resolved at the Reynolds number of 1200. Heat-transfer impediments at the low Reynolds number and low Pu conditions are related with the weak vortical strength and less coolant penetration in the reciprocating thermosyphon, as described previously. Further increases of the Reynolds number to 2500 and then toward 4100 gradually reverse the curvature of $Nu_{\mathrm{ZB}}/Nu_{0,\mathrm{ZB}}$ at each Z spot as seen in the plots of Fig. 12. Clearly, the effects of pulsating number on the reciprocating Nusselt number are strongly dependent on the Reynolds number.

Dependencies of reciprocating buoyancy effect on the flow mechanisms controlled by the Reynolds and pulsating numbers are demonstrated by plotting the n exponents evaluated from Eq. (27) for the entire sets of pulsating and Reynolds numbers examined. A series of Z-wise plots collected in Fig. 13 illustrates the variations of n exponent in Eq. (27) with pulsating number for three the Reynolds numbers tested ($Re = 2100$, 2500, and 4100). In general, the higher values of n exponents develop in the reciprocating thermosyphon with the lower Reynolds number. This result reconfirms the

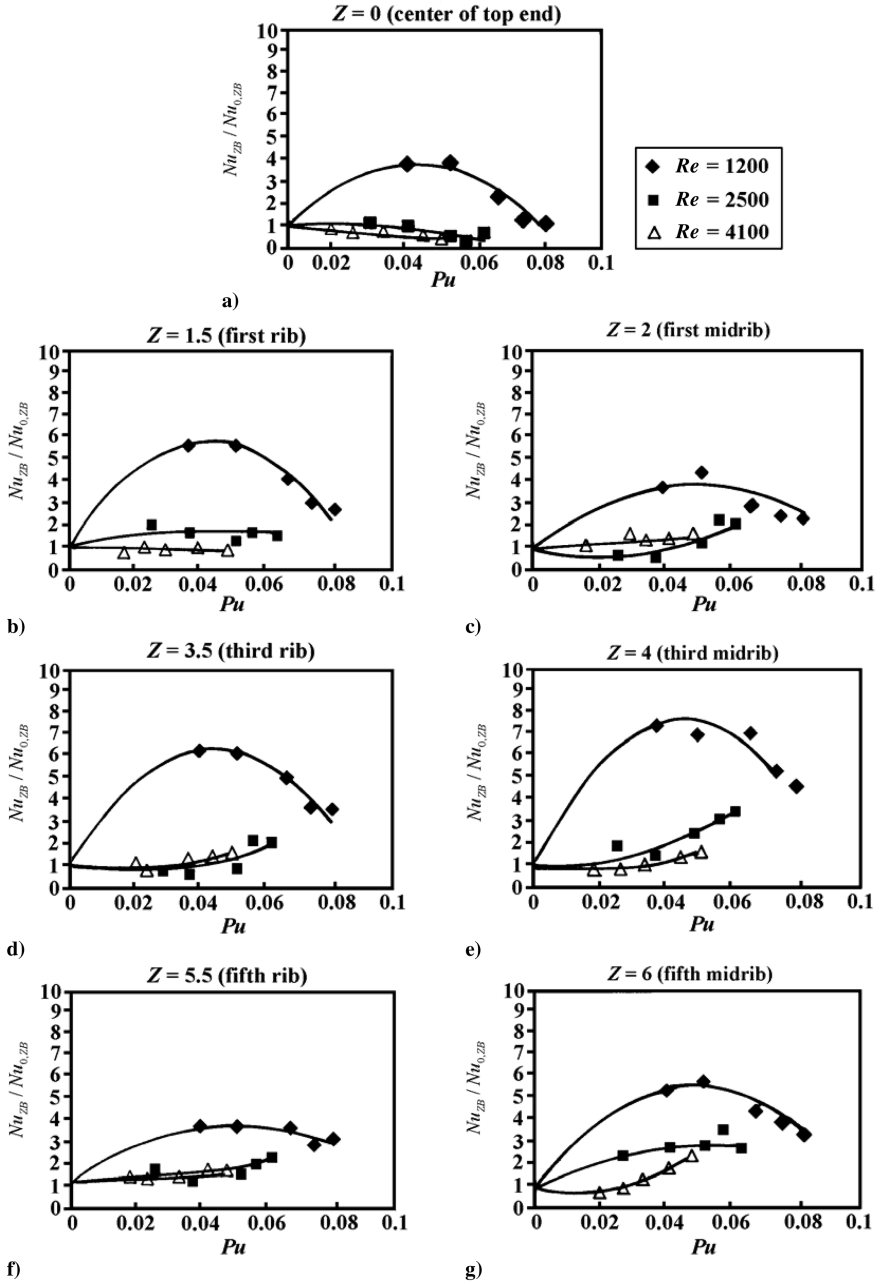

Fig. 12 Variations of $Nu_{ZB}/Nu_{0,ZB}$ ratio with pulsating number at various axial locations.

enhanced dominance of buoyancy impact on heat transfer in the reciprocating thermosyphon as the Reynolds number is reduced. At each selected Reynolds number, the data trend depicted in each plot of Fig. 13 shows the tendency of reduced n exponents as Pu increases. Therefore, the buoyancy effects on heat transfer are weakened in the reciprocating thermosyphon as the pulsating number increases. Above all, the heat-transfer impacts in association with the reciprocating Grashof number are intercorrelated with the Reynolds and pulsating numbers. The complex heat-transfer phenomena developed in the reciprocating antigravity open thermosyphon with piston-cooling applications are revealed by this parametric analysis to demonstrate that the considerable heat-transfer modifications from the static scenarios are due to the individual and interactive effects of Re, Pu, and Gr_p.

Conclusions

This experimental study was devised to reveal the heat-transfer physics in association with the controlling flow parameters identified from a set of flow equations referred to as a reciprocating frame of reference for an antigravity open thermosyphon with two opposite walls roughened by staggered transverse ribs with cooling applications to the piston. Particularly, the interactive and isolated effects of Re, Gr_g, Pu, and Gr_p on heat transfer along the centerline of the rib floor have been studied. In conclusion, the following observations emerge.

1) Local Nusselt numbers in the static thermosyphon increase with the increase of gravitational Grashof numbers for all of the Reynolds numbers tested. Increases of Reynolds number elevate the static heat-transfer rates by enhancing the in-duct vortical strength and coolant penetration, but also produce the attendant reduction in buoyancy effectiveness. The coupled Re-Gr_g effect, which interacts with the rib flows near the sealed end of the thermosyphon, creates the Z-wise zigzag heat-transfer variations. The static Nusselt number correlation, which satisfies both limiting conditions $Re = 0$ and $Gr_g = 0$, is derived to establish the static heat-transfer references for assessing the reciprocating effects on heat transfer.

2) The synergistic Re-Pu-Gr_p effects interacting with the surface ribs considerably modify the heat-transfer scenarios from the static conditions that lead the presented Nu/Nu_0 ratios in the range of

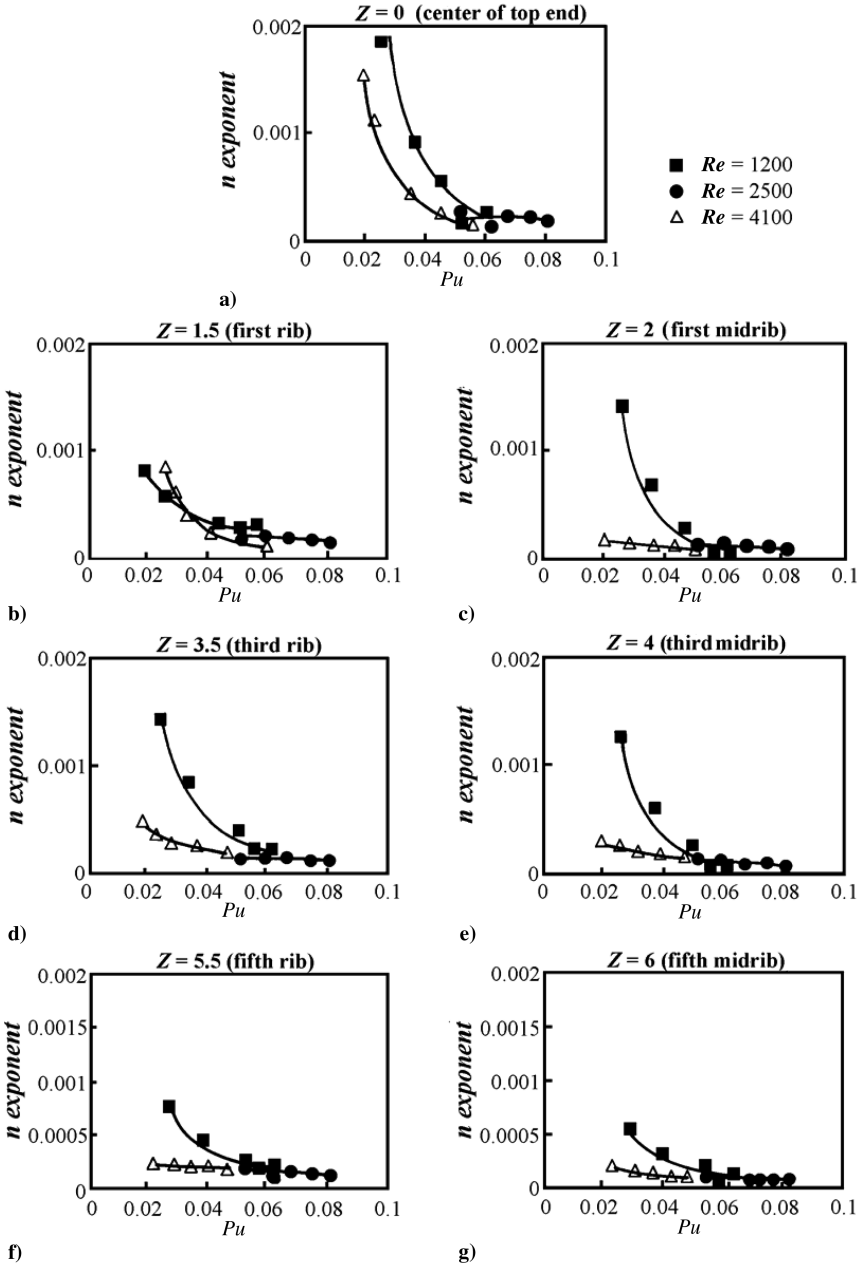

Fig. 13 Variations of *n* exponent with pulsating number at various axial locations.

$0.65 \sim 8$. Heat-transfer impediments developed at the flow conditions, with low Reynolds numbers and low pulsating numbers drew precautions in the design and operating stages for the piston, with its cooling network involving the antigravity open thermosyphons. At high Reynolds and pulsating numbers, the considerable heat-transfer augmentations demonstrate the effectiveness of surface ribs for augmenting the heat transfer in the reciprocating antigravity open thermosyphon.

3) The periodic reciprocating forces indexed by Pu considerably disturb the development of wall flows along the rib floors near the sealed end of the thermosyphon, leading to the diminished zigzag heat-transfer variations in this flow region. The isolated Pu effect at zero buoyancy is dependent on the Reynolds number and Z location. With the flow conditions at low Reynolds numbers of weak vortical strengths and less coolant penetrations, the $Nu_{ZB}/Nu_{0,ZB}$ ratios are initially reduced to be less than unity and then recovered to show considerable enhancements as Pu increases. With high Reynolds numbers, the variation manner of $Nu_{ZB}/Nu_{0,ZB}$ against Pu is reversed from generated low Reynolds numbers, which demonstrates the strong intercorrelations between the pulsating- and Reynolds-number-controlled flow mechanisms.

4) The relative Nusselt number ratio Nu/Nu_0 increases with the increase of the Gr_p value. This isolated Gr_p effect remains persistent over the entire reciprocating rib floor, but its effectiveness is weakened by increasing the pulsating or Reynolds number.

Acknowledgment

This work was funded by the National Science Council, Taiwan, Republic of China, under grant number, NSC 90-2611-E-022-001.

References

[1] Chang, S. W., Su, L. M., Morris, W. D., and Liou, T. M., "Heat Transfer in a Smooth-Walled Reciprocating Antigravity Open Thermosyphon," *International Journal of Thermal Sciences*, Vol. 42, 2003, pp. 1089–1103.

[2] Alkire, J. K., and Deligianni, H., "The Role of Mass Transfer on Anisotropic Electrochemical Pattern Etching," *Journal of the Electrochemical Society*, Vol. 135, 1988, pp. 1093–1100.

[3] Occhialini, J. M., and Higdon, J. J. L., "Convective Mass Transport from Rectangular Cavities in Viscous Flow," *Journal of the Electrochemical Society*, Vol. 139, 1992, pp. 2845–2855.

[4] Fang, L. C., Nicolaou, D., and Cleaver, J. W., "Transient Removal of a Contaminated Fluid from a Cavity," *International Journal of Heat and Fluid Flow*, Vol. 20, 1999, pp. 605–613.
[5] Kwak, H. S., Kuwahara, K., and Hyum, J. M., "Resonant Enhancement of Natural Convection Heat Transfer in a Square Enclosure," *International Journal of Heat and Mass Transfer*, Vol. 41, 1998, pp. 2837–2846.
[6] Kwak, H. S., and Hyum, J. M., "Natural Convection in an Enclosure Having a Vertical Sidewall with Time-Varying Temperature," *Journal of Fluid Mechanics*, Vol. 329, 1996, pp. 65–88.
[7] Antohe, B. V., and Lage, J. L., "Experimental Investigation on Pulsating Horizontal Heating of a Water-Filled Enclosure," *Journal of Heat Transfer*, Vol. 118, 1996, pp. 889–896.
[8] Fu, W. S., and Shieh, W. J., "A Study of Thermal Convection in an Enclosure Induced Simultaneously by Gravity and Vibration," *International Journal of Heat and Mass Transfer*, Vol. 35, No. 7, 1992, pp. 1695–1710.
[9] Fu, W. S., and Shieh, W. J., "Transient Thermal Convection in an Enclosure Induced Simultaneously by Gravity and Vibration," *International Journal of Heat and Mass Transfer*, Vol. 36, No. 2, 1993, pp. 437–452.
[10] Forbes, R. E., Carley, C. T., and Bell, C. J., "Vibration Effects on Convective Heat Transfer in Enclosures," *Journal of Heat Transfer*, Vol. 92, 1970, pp. 429–438.
[11] Cao, Y., and Wang, Q., "Reciprocating Heat Pipes and Their Applications," *Journal of Heat Transfer*, Vol. 117, 1995, pp. 1094–1096.
[12] Gershuni, G. Z., and Lyubimov, D. V., *Thermal Vibrational Convection*, Wiley, New York, 1997.
[13] Han, J. C., Zhang, Y. M., and Lee, C. P., "Augmented Heat Transfer in Square Channels with Parallel, Cross, and V-Shaped Angled Ribs," *Journal of Heat Transfer*, Vol. 113, 1991, pp. 590–596.
[14] Taslim, M. E., Li, T., and Kercher, D. M., "Experimental Heat Transfer and Friction in Channels Roughened with Angled, V-Shaped, and Discrete Ribs on Two Opposite Walls," *Journal of Turbomachinery*, Vol. 118, 1996, pp. 20–28.
[15] Liou, T. M., and Hwang, J. J., "Turbulent Heat Transfer Augmentation and Friction in Periodic Fully Developed Channel Flows," *Journal of Heat Transfer*, Vol. 114, 1992, pp. 56–64.
[16] Roberts, E. P. L., and Mackley, M. R., "The Development of Asymmetry and Period Coupling for Oscillatory Flow in Baffled Channels," *Journal of Fluid Mechanics*, Vol. 328, 1996, pp. 19–48.
[17] Okajima, A., Matsumoto, T., and Kimura, S., "Aerodynamic Characteristics of Flat Plates with Various Angles of Attack in Oscillatory Flow," *JSME International Journal, Series B (Fluids and Thermal Engineering)*, Vol. 41, 1998, pp. 214–220.
[18] Chang, S. W., Su, L. M., Hwang, C. C., and Yang, T. L., "Heat Transfer in a Reciprocating Duct Fitted with Transverse Ribs," *Experimental Heat Transfer*, Vol. 12, 1999, pp. 95–115.
[19] Chang, S. W., Su, L. M., "Heat Transfer of Reciprocating Helical Tube Fitted with Full Circumferential Ribs," *International Journal of Heat and Mass Transfer*, Vol. 44, 2001, pp. 3025–3042.
[20] Morris, W. D., and Salemi, R., "The Effects of Orthogonal-Mode Rotation on Forced Convection in a Circular-Sectioned Tube Fitted with Full Circumferential Transverse Ribs," *AGARD Conference Proceedings*, AGARD, London, Oct. 1992, pp. 527–538; also AGARD Paper 11.
[21] Fann, S., Yang, W. J., and Zhang, N., "Local Heat Transfer in a Rotating Serpentine Passage with Rib-Roughened Surfaces," *International Journal of Heat and Mass Transfer*, Vol. 37, 1994, pp. 217–228.
[22] Johnson, B. V., Wagner, J. H., Steuber, G. D., and Yeh, F. C., "Heat Transfer in Rotating Serpentine Passages with Trips Skewed to the Flow," *Journal of Turbomachinery*, Vol. 116, 1994, pp. 113–123.
[23] Holowenko, A. R., *Dynamics of Machinery*, Wiley, New York, pp. 238–241, 1955.
[24] Kim, J. H., Simon, T. W., and Viskanta, R., "Journal of Heat Transfer Policy on Reporting Uncertainties in Experimental Measurements and Results," *Journal of Heat Transfer*, Vol. 115, 1993, pp. 5–6.
[25] Kim, G. G., and Hyun, J. M., "Buoyant Convection in a Non-Rectangular Cavity with Non-Vertical Insulating Sidewalls," *International Journal of Heat and Mass Transfer*, Vol. 42, 1999, pp. 2111–2117.